









**Strong magnetoelectric coupling at an atomic nonmagnetic electromagnetic probe in bismuth ferrite**

Juliana Schell <sup>1,2</sup> Merlin Schmuck,<sup>2</sup> İpek Efe <sup>3</sup> Thien Thanh Dang <sup>2</sup> João Nuno Gonçalves <sup>5</sup> Daniil Lewin,<sup>2</sup>  
 Marianela Escobar Castillo,<sup>2</sup> Vladimir V. Shvartsman <sup>2</sup> Ângelo Rafael Granadeiro Costa <sup>1,6</sup> Ulli Köster <sup>7</sup>  
 Reiner Vianden,<sup>4</sup> Cornelia Noll,<sup>4</sup> and Doru C. Lupascu <sup>2,\*</sup>

<sup>1</sup>European Organization for Nuclear Research (CERN), CH-1211 Geneva, Switzerland

<sup>2</sup>Institute for Materials Science and Center for Nanointegration Duisburg-Essen (CENIDE),  
 University of Duisburg-Essen, 45141 Essen, Germany

<sup>3</sup>Department of Materials, ETH Zürich, Wolfgang-Pauli-Straße 10, 8093 Zürich, Switzerland

<sup>4</sup>Helmholtz-Institut für Strahlen- und Kernphysik, University of Bonn, 53115 Bonn, Germany

<sup>5</sup>CICECO—Aveiro Institute of Materials and Departamento de Física,  
 Universidade de Aveiro, 3810-193 Aveiro, Portugal

<sup>6</sup>C2TN, Centro de Ciências e Tecnologias Nucleares, Instituto Superior Técnico,  
 Universidade de Lisboa, Lisbon, Portugal

<sup>7</sup>Institut Laue-Langevin, F-38042 Grenoble, France



(Received 12 September 2019; revised 16 November 2021; accepted 14 December 2021; published 4 March 2022;  
 corrected 24 March 2022)

Isolated nonmagnetic substitutional defect ions experience huge coupled electric magnetic interaction in the single-phase multiferroic BiFeO<sub>3</sub>. In the ferroelectric state above the magnetic Néel temperature  $T_N$ , the electric environment generates a single symmetric electric field gradient (EFG) parallel to the electric polarization direction. Below  $T_N$ , a distinct magnetic interaction arises, monitored by the probe nuclei via their magnetic moment. Two magnetic environments arise, given by the relative angle of the local magnetic moment within its easy magnetic plane with respect to the EFG orientation. The angle between field gradient orientation and magnetic field direction is the most stable fitting parameter. The magnetic interaction concomitantly increases the EFG dramatically which reflects an outstandingly large local magnetoelectric coupling. In the set of best fits, two different electric environments form concurrently with two distinctly different local magnetic fields. The magnetic ordering in BiFeO<sub>3</sub> thus completely distorts the electric environment of the nonmagnetic probe nucleus. The implications for the local effect of dopants in BiFeO<sub>3</sub> are discussed. A third probe environment arising independent of temperature is identified and associated with an iron vacancy.

DOI: [10.1103/PhysRevB.105.094102](https://doi.org/10.1103/PhysRevB.105.094102)

## I. INTRODUCTION

Due to the many potential applications in sensors, magnetoelectric memories, spintronics, and photovoltaics [1], much research has been devoted to finding modified versions of bismuth ferrite (BiFeO<sub>3</sub>, in short BFO) which could exhibit considerable macroscopic magnetoelectric coupling. BFO displays ferroelectricity (Curie point  $T_C \approx 1103$  K [2]) as well as antiferromagnetism at room temperature (Néel temperature  $T_N \approx 643$  K) [3,4]. Due to the antiferromagnetic order, global magnetoelectric coupling vanishes practically entirely. As the ordering is very stable for both order parameters and each of them attains large values, it would be a big gain in technology to generate an effective coupling in between them. Many devices could be designed accordingly, particularly magnetoelectric memories at the nanoscale.

Bi<sup>3+</sup> and Fe<sup>3+</sup> cations generate a nonconventional spontaneous electric polarization [5] which is stabilized by the 6s lone pair electrons of Bi, a slight rotation of the oxygen octahedra, and a certain displacement of the iron ion [6]. The rhombohedrally distorted perovskite structure of space group  $R3c$  results from 1 out of 8 possible orientations for polarization along the body diagonals of a pseudocubic unit cell; one such configuration is shown in Fig. 1(a). Within a single ferroelectric domain, the crystal is rhombohedral with polarization along  $[111]_{\text{cubic}} = [001]_{\text{hex}}$ . Below the Néel temperature, the magnetic moments of the Fe<sup>3+</sup> cations interact via superexchange along the Fe-O-Fe bonds at a canting angle of 156° [7–10]. This results in near G-type antiferromagnetism [11]. The spins, however, are not perfectly antiparallel, as there is a weak canting moment caused by the Dzyaloshinskii-Moriya interaction [12]. On top of this local structure, the magnetic moments generate an incommensurate cycloidal structure of magnetic moments in their respective easy planes. The cycloid has propagation direction along any one  $[110]_{\text{cubic}}$  crystal orientation perpendicular to the axis of electrical polarization. Both vectors span up the corresponding easy magnetic plane [11]. For any single polarization direction, three possibilities of orientation of a cycloid

\*doru.lupascu@uni-due.de

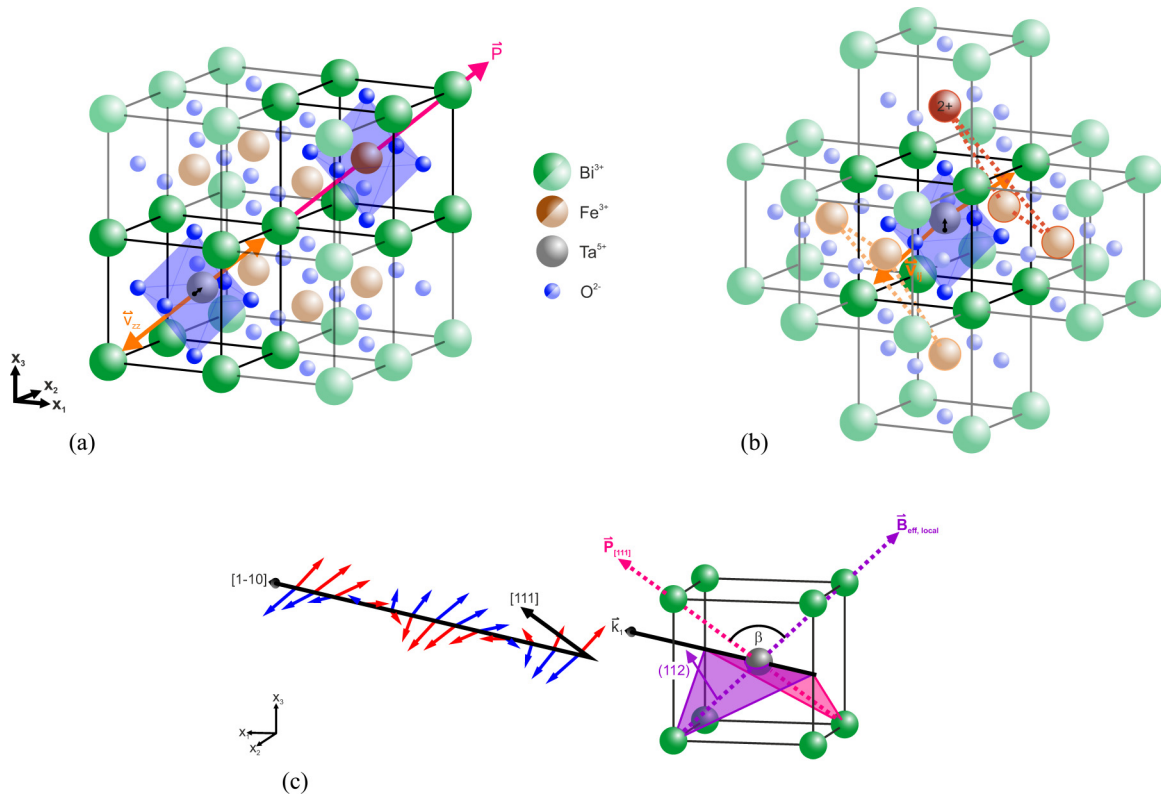


FIG. 1. (a) Orientation of the symmetric electric field gradient (EFG) tensor within the BiFeO<sub>3</sub> lattice. Eight pseudocubic unit cells are shown. The principal orientation axis for the EFG is marked. (b) Sketch of an ion configuration that can yield the asymmetric EFG site 3. One source of asymmetry can be the altered charge state of the adjacent iron or an iron vacancy (see discussion). Any one of the 3 Fe sites connected by a triangle is equivalent with respect to the Ta site symmetry. (c) Configuration for polarization direction, effective magnetic field direction and cycloid orientation as resulting from our data (observe the rotated coordinate system).

direction exist in that respective ferroelectric domain. One is shown in Fig. 1(b).

Ferroelectricity means that external electric fields can reorient the orientation of electric polarization, effectively changing the size of one domain orientation at the cost of reducing the size of others. Lebeugle *et al.* [13] have shown that this switching of a ferroelectric domain is directly accompanied by a concurrent switching of the corresponding magnetic easy plane. Magnetic cycloid propagation across a ferroelectric domain wall is possible because two permitted easy planes intersect for the same cycloid orientation.

The magnetic cycloid is influenced by external constraints. Strain mismatch with substrates in thin films has proven to yield different cycloid configurations [14,15]. Coupling between magnetic and ferroelectric order is strong on the atomic scale [11] but cancels at the macroscopic scale due to the antiferromagnetic order.

Doping is an approach to modify the magnetic structure of BFO [15–20]. The number of systems yielding an effective canting of the antiferromagnetic order due to doping is low, offering only small macroscopic magnetization values [20]. Rare earths have been employed due to their valence compatible with both lattice sites [17,21], as well as manganese or cobalt [22–24]. Nonmagnetic defects also modify the overall behavior by introducing local strain or interrupting the magnetic order at the defect site [25–27]. So far, average techniques have been employed to determine changes of the

global behavior of BFO by doping or geometrical constraints [15].

## II. METHOD

### A. Short intro to the $\gamma\gamma$ perturbed angular correlation technique

Nuclear solid-state techniques like nuclear magnetic resonance (NMR), Mössbauer spectroscopy, or time-differential perturbed  $\gamma\gamma$  angular correlation (TDPAC) spectroscopy monitor the local environment (crystal unit cell and point defects or molecules) of the respective sensitive probe ion. Mössbauer spectroscopy as well as NMR reflects magnetic or electric orders on the local scale for majority ions, e.g., <sup>57</sup>Fe for Mössbauer spectroscopy or protons in NMR. TDPAC detects magnetic fields as well as electric field gradients (EFGs) at tracer probe ions [28]. Typically, these tracers do not alter the properties of the surrounding lattice and only locally represent a defect which can potentially attract electronic charge carriers, vacancies, or interstitial ions. Unlike for Mössbauer spectroscopy, the signal in TDPAC is intrinsically independent of temperature, as no Debye-Waller factor is involved in spectrum formation.

TDPAC uses a  $\gamma\gamma$  cascade in a nuclear radioactive decay. It necessitates three nuclear levels: the excited level, the intermediate level, which is fed from the excited level by emission of a  $\gamma$  quantum  $\gamma_1$ , and a ground level which is

# PAC - Spectroscopy

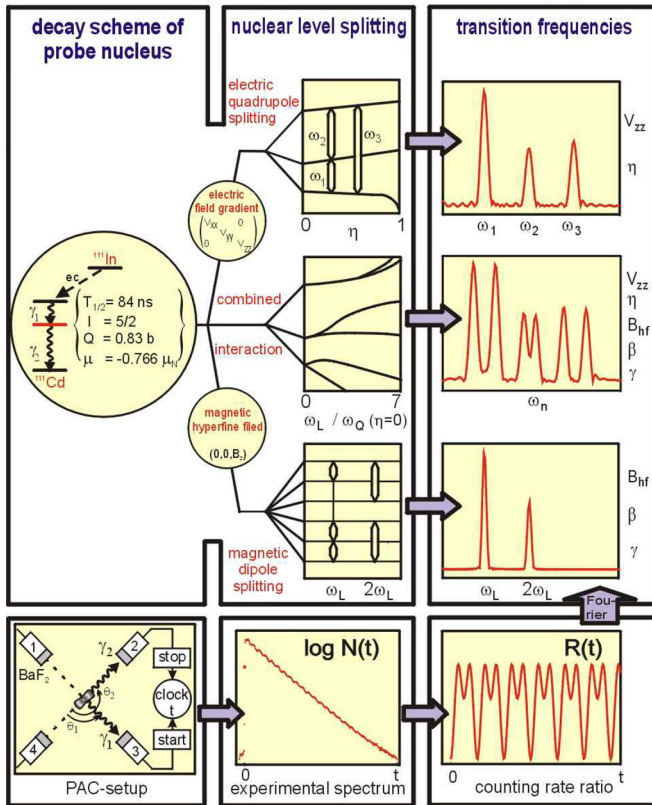


FIG. 2. Sketch showing the splitting of quadrupole frequencies due to the additional magnetic interaction in the case of  $^{111}\text{In}$  [51]. Both interactions may amount to similar precession frequencies which then overall yield a superposition of the now six transition lines. The resulting spectrum looks similar as a damped spectrum but is not. The full theory can be found in Refs. [52,53] (© G. Schatz, University of Konstanz).

reached after emission of a second  $\gamma$  quantum  $\gamma_2$ . An excited level can be created through different nuclear reactions. Due to the quantum mechanical selection rules, the angular emission probability for  $\gamma_2$  is anisotropic in space with respect to the emission direction of  $\gamma_1$ . Both  $\gamma$  quanta are detected in a time-resolved experiment in the nanosecond range for a set of detectors at fixed angles (typically  $90^\circ/180^\circ$ ). During the lifetime of the intermediate level, the nucleus can do a precession movement due to magnetic and electric interactions inducing the time perturbation of the anisotropy, which directly reflects the hyperfine interaction with the electronic and spin environments of the probe nucleus. Depending on the nuclear spin of the sensitive intermediate level, multiple transitions (precession frequencies) arise for a single local environment. In the case of  $I = \frac{5}{2}$ , which is the case here, three nuclear sublevels are split by the hyperfine interaction, yielding three possible precession frequencies  $\omega_1$ ,  $\omega_2$ , and  $\omega_3$ , where  $\omega_3$  is the sum of the other two. Magnetic interaction provides yet an additional splitting of these levels, yielding a total of six levels and accordingly six precession frequencies (transitions), see Fig. 2.

The nuclear probe  $^{181}\text{Ta}$  was fed from the decay of  $^{181}\text{Hf}$  by electron emission from the nucleus. It offers suitable nu-

clear properties and half-life to monitor electric and magnetic interactions. As  $\text{Ta}^{5+}$  as well as  $\text{Hf}^{4+}$  are nonmagnetic, the detected signal reflects the electric and magnetic hyperfine interactions of a nonmagnetic ion  $\text{Ta}^{5+}$  within the surrounding lattice and magnetic structure. Due to their very low concentration, the tracers globally only represent a very weak dopant and do not influence the overall properties of the solid. It is known that doping in the range of 1–3% Ta into  $\text{BiFeO}_3$  [29] (which is very much above the tracer ion concentration used here) does not change the crystal structure. The  $^{181}\text{Hf}$  tracers were implanted at 80 keV at room temperature, yielding an implantation depth of  $\sim 20$  nm and a certain amorphization due to radiation damage. This radiation damage was annealed in a three-step procedure in air (first step: at 773 K for 24 h followed by 873 K for 9 h and 973 K for 10 h) well below the ferroelectric transition (Curie point), placing the tracer ions on well-defined lattice sites in the ferroelectric state of the crystal. As  $\text{BiFeO}_3$  is chemically not very stable above the Curie point, it was important to keep the annealing temperature below  $T_C$ .

## B. Details of the method

In TDPAC, two consecutive  $\gamma$  rays are emitted by the nucleus. Their angular correlation is determined by the properties of the nuclear states involved. The intermediate nuclear state has a finite lifetime. During this lifetime, the nucleus performs precession due to the magnetic interaction of the nuclear spin with the magnetic environment and/or due to the electric interaction of the quadrupole moment of the nucleus with the local EFG tensor of rank two generated by the immediate electrical environment of the nucleus. A distorted electric environment can be generated by low-symmetry crystal lattices or by vicinal point defects. Local magnetic fields yield the magnetic contribution. For a nuclear intermediate state of spin  $\frac{5}{2}$ , which is the case here, three cosinusoidal transition lines are observed due to the electric interaction. If an additional magnetic field is present, these lines are further split by the magnetic field interaction (see Fig. 2). All frequencies superimpose to form the effectively measured TDPAC spectrum. If the local environment is changing dynamically in the time window of measurement, the spectra are damped, which sometimes makes data analysis difficult or impossible.

Hyperfine interactions are extremely sensitive to local phenomena such as spin-state transitions [30], static and dynamic lattice distortions [31,32] including Jahn-Teller distorted local phases [32,33], and defects dynamics [34,35], if the effect is determined by the electrons involved in bonding with the nearest neighbors of the nuclear probe. The method has been used for material characterization for several decades now [36–38]. We nevertheless give a brief and specific introduction to the technique. Further details can be found in Refs. [39–41].

During the lifetime of the intermediate nuclear state, the angular correlation between two consecutive  $\gamma$  rays may be perturbed by the hyperfine interaction from the surrounding electronic charge distribution of the probe nuclei, yielding the perturbation factor  $G_{22}(t)$  [42,43]. Here,  $A_{22}$  is the anisotropy coefficient of the  $\gamma$ - $\gamma$ -cascade. The measured perturbation

function can be approximated as  $R(t) \sim A_{22}G_{22}(t)$ . If there are probe atoms exposed to  $j$  different lattice environments, and each of them creates a characteristic hyperfine interaction at fraction  $f$  of probe atom sites, the perturbation function becomes  $R(t) = A_{22} \sum_j f_j G_{22}^j(t)$ .

The point symmetry at the probe nucleus site depends on the arrangement of its nearest neighbors. The major component of the EFG tensor ( $V_{zz}$ ) can be obtained by the spin-dependent quadrupole frequency  $\omega_Q$ , expressed as

$$\omega_Q = \frac{eQV_{zz}}{4I(2I-1)\hbar}, \quad (1)$$

where  $I$  is the nuclear spin and  $Q$  the nuclear quadrupole moment. For half-integer nuclear spins, the transition frequencies are given by  $\omega_n = 6\omega_Q C_n(\eta)$ . The coefficient  $C_n$  can be numerically calculated for a known asymmetry parameter  $\eta$  [44,45]. All frequency distributions ( $\delta$ ) reported in this paper refer to  $\omega_0$ . The asymmetry parameter  $\eta = |(V_{xx} - V_{yy})/|V_{zz}|$  characterizes the EFG tensor asymmetry and is the only necessary other parameter characterizing the electric environment in the principal axis coordinate system. The orientation of the principal axis coordinate system can only be determined from single-crystal data and is rarely reported.

A last word to clarify notations: generally, one uses the derived quantity  $\nu_Q$  [39,42]:  $\nu_Q = \frac{eQV_{zz}}{h}$ , which is called the electric quadrupole interaction frequency.

For  $I = \frac{5}{2}$  and  $\eta = 0$ , this relates to  $\omega_0$  via  $\omega_0 = 6\omega_Q = \frac{6eQV_{zz}}{4I(2I-1)\hbar} = \frac{3\pi}{10}\nu_Q$  [43].

Below  $T_N$ , the spectra become complex. The transition frequencies are obtained by diagonalizing the complete hyperfine interaction matrix. The Larmor frequency  $\omega_L = -g\mu_N B/\hbar$  is the precession frequency of the nuclear spin around the axis of the magnetic hyperfine field  $B$ . Here,  $g$  denotes the gyromagnetic ratio of the intermediate state and  $\mu_N$  the nuclear magneton. Also,  $B$  is the Euler angle between the principal axis of the electric field tensor  $V_{zz}$  and  $B$ . For BFO, the hyperfine magnetic field represents the combined effect of the transfer of spin density through the iron and oxygen bonds.

Due to the low probe concentration needed for measurement,  $^{181}\text{Hf}$  ( $^{181}\text{Ta}$ ) can effectively act as a spy [46] in bismuth ferrite. Ta is furthermore considered as a dopant with big potential for applications [29]. Ta distorts the Fe-O octahedra [47], reduces the grain size, and can increase the resistivity, allowing for the determination of dielectric properties at room temperature [29]. Just after the  $\beta^-$  decay, the  $\text{Hf}^{4+}$  ion is transformed into a  $\text{Ta}^{5+}$  ion, so that the hyperfine interaction is effectively determined in the  $^{181}\text{Ta}$  excited state. This implies that the  $\text{Ta}^{5+}$  ion determines the details of the hyperfine interaction, but the chemical properties of Hf determine the site selection. In addition, aftereffects [48,49] are not expected for  $\beta^-$  decays. Since bismuth is naturally a diamagnetic element, the magnetic dipole interaction in the magnetically ordered state of  $\text{BiFeO}_3$  arises at the site of the TDPAC probe through the transfer of spin density from  $\text{Fe}^{3+}$ . The effective field at  $\text{Ta}^{5+}$  has been referred to as supertransferred magnetic hyperfine field when

the probes occupy the site of a transition metal ion in similar compounds [50].

### III. SAMPLE PREPARATION

#### A. Ceramic samples

The ceramic samples were produced by the solid-state reaction method using  $\text{Bi}_2\text{O}_3$  and  $\text{Fe}_2\text{O}_3$  powders in stoichiometric amounts. After mixing, the powder was calcined at  $820^\circ\text{C}$  for 3 h. The calcined powder was then pressed into pellets and sintered at 1093 K for 6 h in air, yielding a stable pellet but not a dense ceramic. Figure S2 in the Supplemental Material (SM) [54] shows XRD spectra of the freshly sintered ceramic sample before  $^{181}\text{Hf}$  implantation. Rietveld refinement yields the well-known crystal structure of  $\text{BiFeO}_3$  with space group  $R3c$ , ICSD code 163688 (GOF value 1.8). The lattice parameters are  $a = b = 5.5819 \text{ \AA}$  and  $c = 13.8734 \text{ \AA}$ . A preferred orientation in the planes (104), (006), and (018) is observed. Traces of  $\text{Bi}_{25}\text{FeO}_{40}$  ( $< 2\%$ ) are marked in the spectra. After the thermal treatment, which arises during the several measurements themselves, a second phase ( $\text{Bi}_2\text{Fe}_4\text{O}$ ) evolves due to evaporation of the volatile  $\text{Bi}_2\text{O}_3$ . From independent measurements on similar ceramic samples, we know that this decomposition arises at 973 K only. At all temperatures beneath, no evaporation occurs, and no secondary phase arises. Due to the long half-life of  $^{181}\text{Hf}$ , we did not expose the samples to even higher temperatures because these data were taken late in the decay cycle, and measurement would have taken weeks, changing the sample too much during measurement. We investigated the high-temperature region using another short-lived probe in a separate paper [55].

#### B. Nuclear probe handling

Here, 1.5 mg of  $\text{HfO}_2$  with natural isotopic composition was irradiated for 6 d in a thermal neutron flux of  $10^{15} \text{ n cm}^{-2} \text{ s}^{-1}$  at the high flux reactor of Institut Laue-Langevin (ILL) in Grenoble to produce  $^{181}\text{Hf}$  via the  $^{180}\text{Hf}(n, \gamma)$  reaction. The nuclear probe  $^{181}\text{Hf}$  was implanted at 80 keV at the Bonn Radioisotope Separator (BONIS) [37,56], located at the Helmholtz-Institut für Strahlen- und Kernphysik (HISKP). Since  $\text{HfO}_2$  is too refractory for direct evaporation into the ion source, a stream of  $\text{CCl}_4$  was added to react to volatile  $\text{HfCl}_4$  which was injected into the ion source, forming  $\text{Hf}^+$  ions after ionization. After mass separation, the  $^{181}\text{Hf}$  ions (corresponding to an activity of  $\sim 200 \text{ kBq}$  per the sample) were implanted over an area of  $\sim 5 \times 5 \text{ mm}^2$ , i.e., the real density of  $^{181}\text{Hf}$  was  $< 10^{12} \text{ atoms/cm}^2$ . The selected  $\gamma$ - $\gamma$  cascade of (133–482) keV is populated via the  $\beta^-$  decay of  $^{181}\text{Hf}$  and has been used to measure the hyperfine interactions on the 482 keV ( $\frac{5}{2}^+$ ) state of  $^{181}\text{Ta}$ , with a quadrupole moment of  $Q = +2.28(2) \text{ b}$  [57,58] and anisotropy coefficients  $A_{22} = -0.288$ ,  $A_{24} = -0.062$ ,  $A_{42} = -0.318$ , and  $A_{44} = -0.076$ .

Following implantation, radiation damage was annealed in air up to temperatures of 973 K in three steps: at 773 K for 24 h followed by 873 K for 9 h and 973 K for 10 h. The TDPAC measurements were carried out at ISOLDE-CERN [37]. Above laboratory temperature, a digital setup [59] was employed using a conventional furnace. The machine

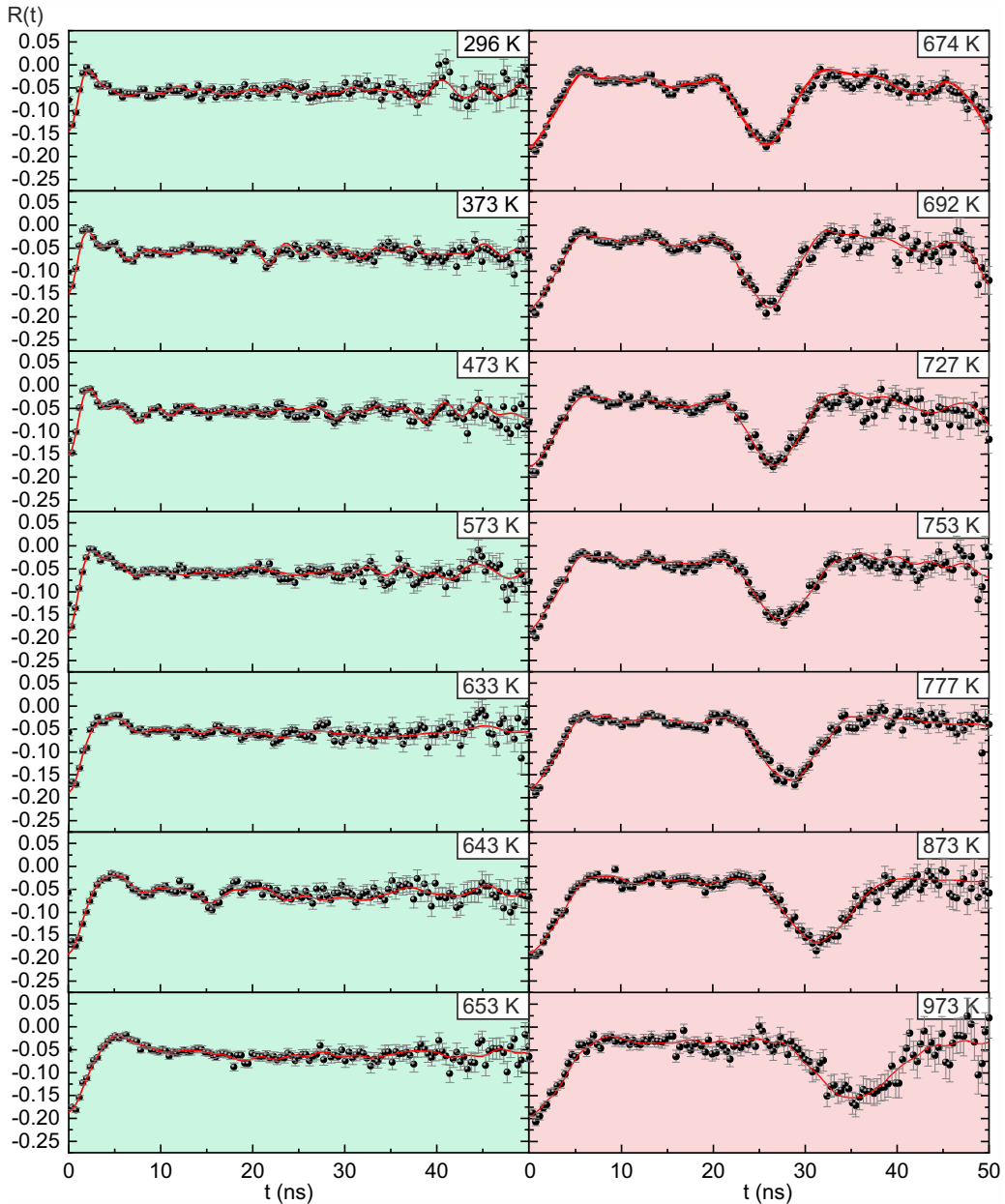


FIG. 3. Time-differential perturbed  $\gamma\gamma$  angular correlation (TDPAC) spectra measured as a function of temperature below (left) and above (right) the Néel temperature  $T_N$ . Least-squares fits of the hyperfine parameters are represented by the red solid lines. Fourier transforms can be found in the Supplemental Material [54]. Green background denotes spectra in the antiferromagnetic temperature range, red the purely ferroelectric one.

was equipped with six conical  $\text{LaBr}_3\text{Ce}$  detector scintillators with a time resolution of 0.7 ns (full width at half maximum). The measurement at each temperature lasted from 3 to several hours. The thermal treatments at 500, 600, and 700 °C were performed during the measurements. Below room temperature, a conventional digital setup [59] coupled to a cold finger system was used. It contains six 1" x 1" cylindrical  $\text{CeBr}_3$  detector scintillators with significantly improved light yield and consequently increased pulse height, keeping equally good time resolution but much better energy resolution of 4% at 511 keV. The theoretical perturbation functions were fitted to the obtained spectra using the NIGHTMARE [60] software to extract the hyperfine parameters.

#### IV. RESULTS

Figure 3 displays the spectra taken at different temperatures above (red background) and below (green) the magnetic phase transition at the Néel temperature  $T_N$ . It is very well visible that the spectra change drastically once the magnetic interaction additionally affects the probe ions.

Fitting the spectra below  $T_N$  necessitates two different environments of the  $^{181}\text{Ta}$  probe. We call these sites 1 and 2 in the following. They develop from a single electric environment in the purely ferroelectric crystal state above  $T_N$ . Thus, experimental sites 1 and 2 denote two environments to the same crystallographic lattice site which will be simply labeled site 1 above  $T_N$ .

The material is in its paramagnetic ferroelectric state above the magnetic Néel temperature  $T_N$ . Two static nuclear quadrupole interactions are observed in the spectra (right column of Fig. 3). Site 1/2 is symmetric ( $\eta \approx 0$ ) and represents  $> 80\%$  of the observed probe nuclei. Site 3 is highly asymmetric ( $\eta > 0.8$ ) and of very high frequency.

For site 1/2, the EFG values decrease with rising temperature. They stem from substitutional  $^{181}\text{Hf}$  on the Fe lattice site (see discussion below). Site 1/2 is roughly symmetric and thus substitutional without any further point defects associated with it. The EFG 1 reflects the electric environment of the probe. This encompasses the crystal structure (i.e., the ionic positions) but also deformations of the electronic shells differing from spherical symmetry. It is known that polarization of the ferroelectric state in  $\text{BiFeO}_3$  is largely constituted by the deformation of the Bi  $6s$  electrons. This obviously also changes the electric environment of the probe ion considerably. Thus, the EFG will change with the formation of polarization below the ferroelectric phase transition and become temperature dependent accordingly. The EFG value  $V_{zz}$ , which is proportional to the observed quadrupole frequency  $\omega_Q$ , follows the temperature dependence of the square of polarization. Our density functional theory (DFT) calculations also show that the EFG is proportional to the square of the order parameter polarization for Fe on the Fe site (see Sec. V). Like  $\text{BaTiO}_3$ , but unlike  $\text{PbTiO}_3$  [61],  $\text{BiFeO}_3$  shows a linear dependence of the EFG values on  $P^2$ . The inset of Fig. 4 shows these calculation results. The Landau theory affords a root dependence of spontaneous polarization of the crystal on temperature up to  $T_C$  [62]; the EFG thus should follow [63]

$$V_{zz} = \xi P_s^2 = \xi \frac{\beta}{2\gamma} \left[ 1 + \sqrt{\frac{1}{4} - \frac{\chi_0^{-1}\gamma}{\beta^2}(T - T_C)} \right], \quad (2)$$

using the definitions of the Landau expansion coefficients  $\alpha = \chi_0^{-1}(T_0 - T)$ ,  $\beta$ , and  $\gamma$  according to the standard version [62] (see fits in Fig. 3). The temperature dependence of  $\alpha$  reflects the Curie-Weiss law, and  $T_0$  is the Curie point (not the phase transition Curie temperature  $T_C$ , which for a first-order phase transition is given by  $T_C = T_0 + \frac{3}{16} \frac{\beta^2}{\chi_0^{-1}\gamma}$  [62]). The change of the local EFG at the probe site is a result of the change in polarization. To understand how the change in polarization with temperature is related to the change of  $V_{zz}$ , we used the experimental data for  $P_s$  collected by Karpinsky *et al.* [64] for fitting Eq. (2), which directly results from the Landau theory [63]. The proportionality  $V_{zz}^{\text{Ta}} = \xi P_s^2$  was fitted to the PAC parameters from the high-temperature range of Fig. 4, yielding  $\beta/\gamma = 3102 (\mu\text{C}/\text{cm}^2)^2$ ,  $\chi_0^{-1}/\beta = 4.6 (\text{cm}^2/\mu\text{C}^2)/\text{K}$ , and  $\xi = [(0.00145 \pm 3 \times 10^{-5}) \text{Vcm}^2/(\mu\text{C})^2] P_s^2$ . Thus, the probe ion  $\text{Ta}^{5+}$  experiences the same temperature dependence of the locally active EFG as would apply to  $\text{Fe}^{3+}$  on the Fe site, which we deduced from the DFT model to be proportional to  $V_{zz}^{\text{Fe}} = \zeta P_s^2$  ( $\zeta \neq \xi$ , see Fig. 4 inset).

Due to its ion size,  $\text{Hf}^{4+}$  occupies the iron site (ion radii:  $\text{Hf}^{4+}$  is 0.085 nm,  $\text{Ta}^{5+}$  is 0.070 nm,  $\text{Fe}^{3+}$  0.064 nm, and  $\text{Bi}^{3+}$  0.117 nm [65]). This is common understanding in the

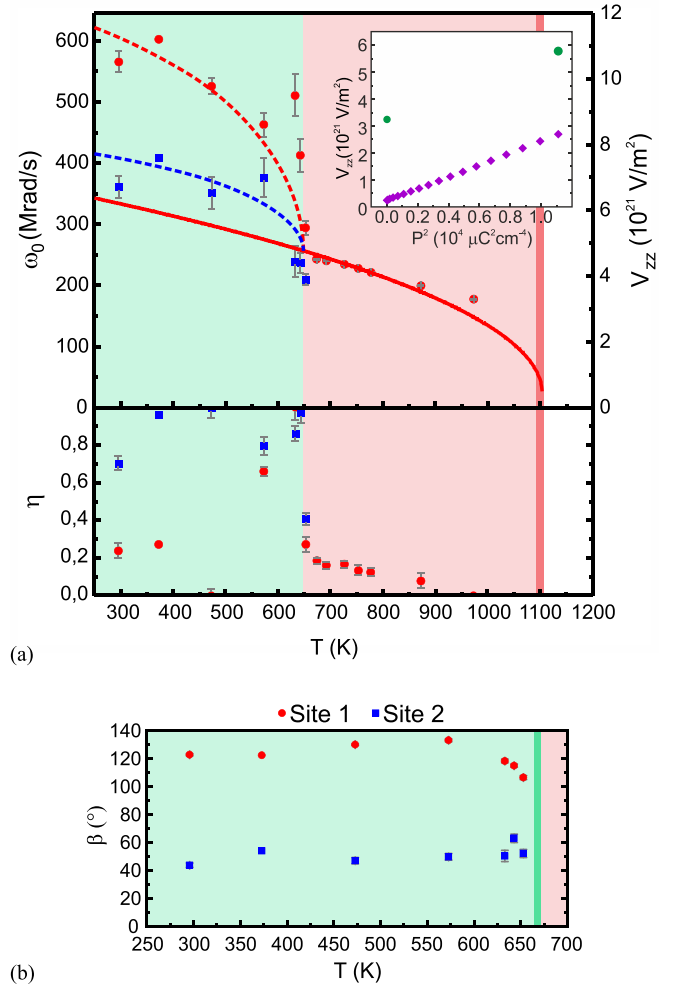


FIG. 4. Electric field gradient (EFG) fitting parameters at the substitutional  $^{181}\text{Ta}$  ion. Two sites are identified. (a) Site 1 is entirely symmetric above  $T_N$  and below  $T_C$ . The EFG reflects the polar ferroelectric order parameter. The lines represent a Landau fit for a first-order phase transition where  $V_{zz}$  is proportional to  $P^2$  according to Eq. (1).  $P$  stems from independent macroscopic data. The ferroelectric phase transition is of highly first order arising at  $T_C = 1103$  K. The dotted fit lines represent the onset of magnetic order which strongly changes the electric environment of the  $^{181}\text{Ta}$  probe ion. The chosen curve shape represents a potential proportionality to the macroscopic magnetic ordering according to the Brillouin function. The asymmetry of the site changes near  $T_N$ . The inset shows density functional theory (DFT) calculations of the EFG. Its strength is proportional to the square of the order parameter, which is polarization, for Fe on the Fe site. To not be limited by the finite unit cell size in the model, we determined the field gradient in the unperturbed lattice without  $^{181}\text{Ta}$  introduced into the model for obtaining the temperature dependence of the local environment in a first step. The two green points are calculation results with Ta in supercells for the  $R\bar{3}c$  and  $R3c$  structures (see text). (b) Beneath  $T_N$ , sites 1 and 2 differ in the angle  $\beta$  of magnetic interaction with respect to the EFG principal axis. The EFG strength and symmetry differ for both sites. The value of the angle persistently lies  $\sim 120^\circ$  for site 1 and  $40^\circ$  for site 2.

literature [29]. For detailed arguments, see the SM [54]. In the purely ferroelectric phase, the sensitive state in  $\text{Ta}^{5+}$  experiences the vicinity of the  $\text{Bi}^{3+}$   $6s^2$  lone pair electrons, which

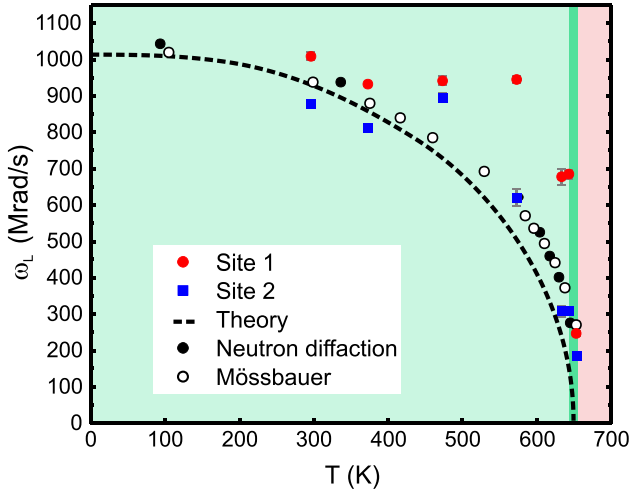


FIG. 5. The magnetic Larmor frequency  $\omega_L$  from the perturbed  $\gamma\gamma$  angular correlation (PAC) data as a function of temperature. Normalized neutron diffraction and Mössbauer data are shown for comparison. Site 2 nearly follows the Brillouin function of the antiferromagnetic order parameter [69], while site 1 experiences an enhanced local magnetic field compared with the sublattice magnetization value near  $T_N$ . The PAC is sensitive to the local magnetic field only and not to the bulk average. The signal is thus large despite antiferromagnetic order. Neutron and Mössbauer (from the intrinsic iron ion) data are normalized to be comparable with the PAC precession frequency of the Ta ion. The width of the green bar reflects the temperature uncertainty in comparing calorimetric to PAC data. Mössbauer data stem from Ref. [65], neutron data from Ref. [69].

constitute the major part of crystal polarization. As  $\text{Ta}^{5+}$  is positively charged with respect to the  $\text{Fe}^{3+}$ ,  $\text{Ta}^{5+}$  is attracted to the lone pair electrons of Bi, which are oriented axially along  $[111]_{\text{cubic}} (= [001]_{\text{hex}})$ . As the lone pair (6s) electrons show significant probability of occupancy of volumes away from the Bi nucleus site, we assume that a certain hybridization arises to the vacant Ta 6s orbitals [Fig. 1(d)]. The large EFG then stems from the deformation of the electronic shell of  $\text{Ta}^{5+}$  due to the vicinity of  $\text{Bi}^{3+}$  and the concurrent partial hybridization.

A strongly asymmetric site 3 can be associated to a charged point defect or represents Ta ions located at a domain wall [66]. As the EFG is well defined, localization at a grain boundary is not possible, which would yield a broad distribution of values. As is estimated from modeling (see Sec. V), an adjacent point defect is the most likely setting. The influence of the order parameter on EFG 3 is experimentally practically void (Fig. 5). The adjacent defect dominates the asymmetry. Nevertheless, a change in EFG due to the changing order parameter is visible in the data near  $T_N$ , which we consider to be due to fluctuations near the instability point  $T_N$ . If site 3 were considered to reside at a ferroelectric domain wall, the change in order parameter would thus vanish at the wall. This is unlikely because the domain wall directly reflects the interface between two parts of the crystal of well-defined order parameter relation. The DFT model suggests that the adjacent defect is an iron vacancy. We therefore assign localization of an iron vacancy near the probe ion for site 3.

In the antiferromagnetic state below  $T_N$ , the magnetic signal component is superimposed on the electric signal, yielding combined interaction. Due to the high quality of the TDPAC spectra, the magnetic and electric signals can be separated from the fits.

#### A. Effect of magnetic order on site 1/2

Figure 5 shows the temperature dependence of the antiferromagnetic order parameter, the sublattice magnetization, via the Larmor frequency  $\omega_L$  for both sites 1 and 2. It steeply vanishes at  $T_N$  ( $T_N = 655 \pm 10$  K, Mössbauer data yield  $T_N = 654.9$  K [67]). The Brillouin function from Ref. [68] is known to represent the change of macroscopic and local magnetization, as monitored by neutron data or Mössbauer spectroscopy on the lattice ion iron. We evaluated whether the magnetic signal in PAC  $\omega_L$  also follows the sublattice magnetization value (hatched line in Fig. 5, original figure, see Fig. S9 in the SM [54]). As the precession frequencies due to electric and magnetic coupling are similar, none of both can be considered as perturbation of the other, and the fully coupled quantum mechanical fit of the EFG data must be used. Within the measured spectra, the steep drop in the initial data points in the time domain (Fig. 3), particularly for the lower temperatures, is a result of the similar frequencies and is not due to damping or fluctuations. Only near  $T_N$ , the spectra are smeared out reflecting fluctuations. The coupled magnetic-electric fits yield the EFG ( $v_q$  and  $\eta$ ) as well as the local magnetic precession frequency  $\omega_L$  at high precision. Thus, if changes in the EFG are found, they do reflect changes of the electric environment even below the magnetic phase transition temperature. This electric environment changes considerably beneath  $T_N$  (see Fig. 3), amounting to  $\sim 30/100\%$  of the ferroelectric distortion due to the electric polarization of the lattice itself (the ferroelectric distortion itself is extrapolated from the values from above  $T_N$ ). The magnetically induced change in  $\omega_0$  roughly scales with  $\omega_L$ :  $\Delta\omega_0 = \zeta\omega_L$  for both sites (see approximate lines in Fig. 4), which indirectly is a magneto-electric coefficient. Magnetic ordering thus largely displaces the Ta ion from its original position. At low temperature, the EFG (site 1) is strongly enhanced. It is asymmetric but not excessively. A second local electric environment emerges which is strongly distorted, namely, the EFG exhibits high asymmetry with a lesser change in field gradient value (site 2). These two changes can result from an actual shift of the Ta ion in its octahedron or a reordering of the directly adjacent electron density. Likely, both effects occur concurrently. Thus, on the scale of the (crystallographic) unit cell, the changes in electrical ordering due to magnetic ordering are huge. This reflects the local magnetoelectric coupling between the spin ordering of  $\text{Fe}^{3+}$  and the ferroelectric ordering of  $\text{Bi}^{3+}$ . This local magnetoelectric coupling yields a 100% change of polarization for site 1 and  $\sim 30\%$  for site 2 at the atomic scale, the largest magnetoelectric coupling reported so far. Due to the antiferromagnetic structure, the effective coupling nearly cancels on the scale of the magnetic unit cell, which is bigger than the crystallographic one and includes the antiparallel magnetic spins. Thus, if  $\text{BiFeO}_3$  were a ferromagnetic and not an antiferromagnetic material, it would be the dream candidate for magnetoelectric coupling, which

we, here, probe locally. Once the magnetic order is fully developed and fluctuations are no longer relevant (well beneath  $T_N$ ), the EFG returns to its original orientation, yielding a low electric asymmetry on site 1 and a stable asymmetry for site 2. The data show that an effective maximum magnetic field strength of  $\sim 16$  T ( $\omega_L = 1000$  Mrad/s) is encountered at the probe site 1.

A comparison with Mössbauer data [69] shows that the intrinsic probe ion  $\text{Fe}^{3+}$  does not experience such a strong coupling as does the nonmagnetic ion  $^{181}\text{Ta}^{5+}$ . This implies that the superexchange between the iron ions stabilizes the  $\text{Fe}^{3+}$  on its lattice location and reduces its coupling to the ferroelectric distortion, while for  $\text{Ta}^{5+}$ , a very strong coupled interaction is found in our experiments.

### B. Symmetry of site 1

The most robust fitting parameter in our data is the angle between the EFG orientation, namely, the  $z$  axis of the respective local principal axis coordinate system of the diagonalized tensor and the local magnetic field direction [Fig. 3(b)]. For a positive  $V_{zz}$ , which determines the positive  $z$  axis of the principal coordinate system of the EFG tensor, the local magnetic field is angled at  $\beta = 120^\circ$  with respect to this  $z$  axis (not to be confused with the Landau coefficient  $\beta$ ). This angle practically does not vary with temperature. According to neutron diffraction data by Lebeugle *et al.* [13], the magnetic cycloid of BFO resides in  $\{112\}$  planes, which are spanned up by the ferroelectric polar direction  $\langle 111 \rangle_c$  and the propagation vector of the cycloid  $\langle 110 \rangle_c$ . For each polar direction, three specific propagation directions are permitted, one of which will occur for each cycloid. Lebeugle *et al.* [13] associate the easy magnetic plane with the polar direction under  $60^\circ$ . Considering Fig. 1(c), our data define that, if the  $z$  direction of the EFG tensor is parallel to  $\vec{P}$ , then the direction of  $\vec{B}$  is under  $120^\circ$  slightly larger than the crystallographic angle of  $109^\circ$  shown. Thus, sites 1 and 2 represent the ordering of electric and magnetic interaction in the respective two easy planes for the magnetic order. Different from the neutron data by Lebeugle *et al.* [13], our data show that the easy magnetic plane associated with that polarization direction does not contain  $\vec{P}$  itself. The  $z$  axis could also show along  $-\vec{P}$ . Then the direction of  $\vec{B}$  would also be reversed but still reside in the same easy plane. The case of site 1 is illustrated in Fig. 1(c), where we show the two possible easy planes for magnetization and one direction of  $\vec{P}$ .

The respectively other angle between the field gradient tensor orientation and the magnetic field vector we observe is under  $40^\circ$  for site 2. This is accompanied by a large asymmetry of the field gradient. Reasonably, this reflects a magnetic moment in the respectively other magnetic easy plane. Also in this latter case, a distinct angle is observed; as said earlier, this is the most robust fitting parameter. Thus, PAC suggests that there is no preferred orientation of magnetization with respect to polarization, different from the final assumption by Lebeugle *et al.* [13].

For thin films, it has been reported that epitaxial strain can stabilize other cycloid variants, e.g., with the cycloid plane making an angle to the polarization direction [14,70,71]. Our situation is different from the biaxial strained films. A defect

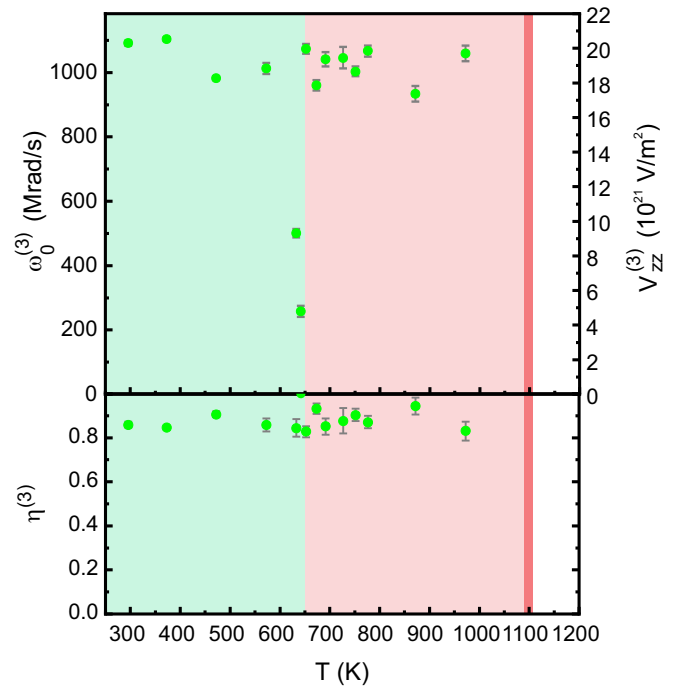


FIG. 6. The temperature dependence of the electric hyperfine parameters for the defect-associated site 3. Its properties are practically independent of temperature. Merely the fluctuations near  $T_N$  generate an apparently very different field gradient value.

ion creates a 3D strain in its immediate neighborhood, equivalent to a positive or negative hydrostatic pressure, depending on the relative ion size with respect to the ion it replaces. However,  $\text{Ta}^{5+}$  and  $\text{Fe}^{3+}$  have practically the same ionic radii in the octahedral environment, 64 and 64.5 pm, respectively [65]. Therefore, one should not expect a strong effect from the mechanical point of view. We thus consider that the visible strong electric distortions largely stem from deformation of the electron density around the probe atom.

In general, the G-type antiferromagnetic order in BFO is slightly canted and does not fully cancel. This is due to the Dzyaloshinskii-Moriya interaction. Two canted (antiferromagnetic) spins yield a vector sum magnetization which is very small and oscillates with the same periodicity as the spin cycloid. This sum component is nearly perpendicular to the overall spin orientations of the cycloid within the easy planes. If the Ta probe would experience this effective sum field, it would have to be oriented under  $90^\circ$  with respect to the polar axis and the cycloid propagation direction. We do not observe  $90^\circ$ , so the selection of each spin state near the Ta probe ion is independent of the second-order Dzyaloshinskii-Moriya interaction and directly correlated with the primary-order parameter, namely, the spins of the antiferromagnetic sublattice itself.

### C. Site 3

Site 3 is highly distorted and assumes a different symmetry (Fig. 6) due to an adjacent defect. The properties of this site are practically independent of temperature. No influence of global ordering on the field gradient values is found. Also, the fraction of site 3 practically does not vary. The nearby defect



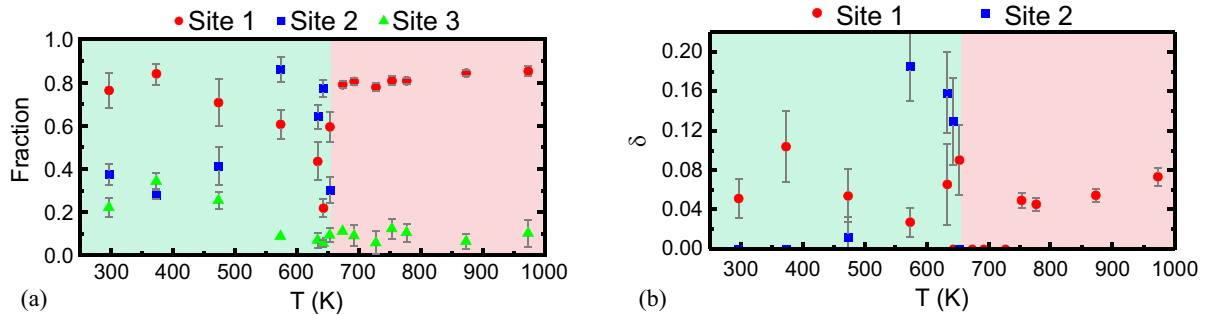


FIG. 7. Temperature dependence of the hyperfine frequency distribution width ( $\delta$ ) and the normalized site-occupation fractions of the  $^{181}\text{Ta}$  probes. Sites 1 and 2 represent the identical lattice substitutional Fe lattice site. They yield different environments only once magnetic interaction sets in.

(very likely an Fe vacancy, see Sec. V) reduces the effect of the magnetization on the distortion of the electric environment of the probe ion. This indicates that the most likely defect environment is a defect. Hf and Ta are soft dopants in BFO. Electrochemistry forbids that they associate with an oxygen vacancy (see SM [54]). Interstitial sites are practically impossible in the perovskite structure for a tolerance factor  $t \sim 1$  [72]. As is shown from electrochemistry in the SM [54], an Fe vacancy is most likely present at site 3. A high-frequency contribution like site 3 was inevitable to fit the data over the entire temperature range. As a pure EFG was sufficient to fit the data, no additional magnetic interaction was used as a free parameter in the fits. It would have inferred a too large error bar.

#### D. Additional fit parameters

The site occupancy is a parameter in PAC that displays how many of the ions occupy certain hyperfine interaction environments. Often, these are different lattice sites or adjacent vacancies or interstitials. Similarly, the association of an electronic defect will also create a “new” site. Thus, evaluating the site assignment can be a difficult task because recharging can happen for different true lattice sites at different temperatures.

The fits to our data below the Néel temperature show that an electrically single site above  $T_N$  splits into two effective environments beneath. For site 1, the hyperfine frequency distribution width [Fig. 7(b)] increases up to  $T_N$ , meaning an increased uncertainty or fluctuations of the local environment. This is typical for a transition of second order between two phases [73]. The spread of the order temperature has also been observed by TDPAC for a distribution of Curie temperatures for several compounds [73]. The site assignment shows that, near  $T_N$ , a larger uncertainty arises in site assignment [Fig. 7(a)]. This correlates well with the distribution width [Fig. 7(b)]. The fraction of the defect-associated site 3 does not change much over temperature. We thus assume that the associated defect is stable over the entire temperature range.

#### V. MODELING

Understanding the local environment of a probe ion can be based on general symmetry arguments, but the strength of the interaction is determined by the very local electric and magnetic environments. In the following, we will give estimates

on the interaction strength based on DFT calculations. As a foreign probe will alter a supercell much, care must be taken in interpreting the data because a single probe ion in such a supercell effectively corresponds to a high doping level, which in experiment is not the case. Evidently, DFT runs at 0 K, which must be considered in interpreting high-temperature data. We attained a fair match between the model and the experimental data.

We used the projector augmented wave method [74] as implemented in the VASP code [75]. The generalized gradient approximation of Perdew-Burke-Ernzerhof (GGA-PBE) was sometimes used [76], but while this approximation yields a rough estimate, it may not include the correct amount of electron localization. To correct the electronic description, we also used the PBEsol version [77] with an added Coulomb repulsion term to the localized Fe  $3d$  orbitals ( $U_{\text{eff}} = 2$  eV), using the Dudarev approach [78]. This is consistent with a recent study in  $\text{BiFeO}_3$  [79], which recommended that “a  $U$  value of at most 4 eV be applied to the Fe  $d$  orbitals in BFO,” using PBE. We have used PBEsol +  $U$ , which usually requires a slightly smaller  $U_{\text{eff}}$  for similar results in comparison with PBE +  $U$ ; therefore,  $U_{\text{eff}} = 2$  eV seems a reasonable choice. The PBE EFGs are shown in three cases, as the left values in Table I (when there is  $> 1$  value), showing results like PBEsol +  $U$ . The cases with two results (PBE and PBEsol +  $U = 2$  eV) show that the exact choice of the  $U$  value for the Ta EFG is not very significant since the resulting  $V_{zz}$  values are relatively close.

The calculation is spin polarized and ferromagnetic (an approximation to the paramagnetic state found at the measured temperatures). We used an energy cutoff of 950 eV for the plane waves and a  $7 \times 7 \times 3$  Monkhorst-Pack  $\Gamma$ -centered k-points grid for the conventional cell. For the  $2 \times 2 \times 1$  supercells, we used an energy cutoff of 400 eV and  $3 \times 3 \times 2$  k-points. The lower cutoff should be enough for reasonably good accuracy, as seen by tests in the smaller cell.

Two settings were followed in modeling. The first concerns the  $\text{BiFeO}_3$  crystal without a defect. This was with the goal to understand the dependence of the local EFG on the macroscopic polarization state of the sample. The second involves the incorporation of Ta as the nuclear probe ion. Since the calculations are periodic, we should increase the supercell to remove interaction between Ta defects. Therefore, while the periodic functions in the model should describe the effect of

TABLE I. Simulated EFG parameters for different Ta defect configurations (two supercell sizes) and experimental values (right column). In cases with two values in the model, the first one was obtained with GGA-PBE, while the second one was obtained with GGA + PBEsol +  $U = 2$  eV.

|  | $1 \times 1 \times 1$           |           | $2 \times 2 \times 1$           |        | Experimental values @ RT         |                            |
|--|---------------------------------|-----------|---------------------------------|--------|----------------------------------|----------------------------|
|  | $V_{zz}(10^{21} \text{ V/m}^2)$ | $\eta$    | $V_{zz}(10^{21} \text{ V/m}^2)$ | $\eta$ | $V_{zz} (10^{21} \text{ V/m}^2)$ | $\eta$                     |
| Ta: Bi   | 19.01                           | 0         |                                 |        |                                  |                            |
| Ta: Fe   | 7.26                            | 0         | 6.21/5.78                       | 0      | 10.52 (0.32)<br>6.73 (0.34)      | 0.24 (0.04)<br>0.70 (0.04) |
| Ta: Fe ( $R\bar{3}c$ )                                     |                                 |           | 3.93/3.37                       | 0      |                                  |                            |
| Ta : Fe + $V_O$  | 33.71                           | 0.36      | 40.96                           | 0.05   |                                  |                            |
| Ta : Fe + $V_{Bi}$   |                                 |           | 10.99                           | 0      |                                  |                            |
| Ta : Fe + $V_{Fe}$   |                                 |           | 5.64                            | 0.91   | 20.30 (0.16)                     | 0.86 (0.01)                |
| Ta: Fe ( $Pnma; 2 \times 1 \times 2$<br><i>supercell</i> ) | -5.75/-7.17                     | 0.76/0.76 |                                 |        |                                  |                            |

the EFG at the Fe site for Fe, well a larger error is expected for the model including the Ta probe as a defect. It turns out that the resulting ‘‘concentration’’ of Ta in the lattice yields metallic behavior. Thus, a different modeling approach became necessary to be able to determine the  $V_{zz}$  dependence on polarization.

(1) Fe on Fe site: We calculated the electric environment of Fe on the Fe lattice site according to the same scheme as conducted in Ref. [61]. The behavior of  $V_{zz}$  as a function of the polarization of the lattice follows the same trend as it does for  $\text{BaTiO}_3$ , namely, a linear dependence on  $P^2$  [see the purple points of Fig. 3(a)]. We used this dependence for estimating the effect of the temperature dependence of the macroscopic polarization on  $V_{zz}$  [see Eq. (2)].

(2) Ta probe included: We calculated the EFG of the Ta probe at different sites to arrive at a probe site assignment for the measurements based on the comparison of calculated with experimental values. We also performed the Ta:Fe calculations with the  $R\bar{3}c/R3c$  structures to estimate the variation of  $V_{zz}$  with  $P$  [as shown in the green points of Fig. 3(a)].

We have first considered a Ta impurity in one hexagonal unit cell (with 5 f.u., and lattice parameters  $a = 5.575 \text{ \AA}$ ,  $c = 13.868 \text{ \AA}$ ). Specifically, we considered two substitutional situations at either Bi or Fe sites. In the first case, we obtained  $V_{zz} = 19.01 \times 10^{21} \text{ V/m}^2$ , while in the second case, we obtained  $V_{zz} = 7.26 \times 10^{21} \text{ V/m}^2$ . The comparison of the calculations with the lowest temperature experimental frequencies indicate that Ta occupies the Fe site. We have also considered the situation where the Ta is substitutional at Fe with the nearest O neighbor removed (Ta : Fe +  $O_v$ ), which results in  $V_{zz} = 33.71 \times 10^{21} \text{ V/m}^2$  and  $\eta = 0.36$ . Table I summarizes the simulated hyperfine parameters for the  $1 \times 1 \times 1$  conventional cells and for the  $2 \times 2 \times 1$  supercells. This value is considerably larger when compared with experiment, and the association of an oxygen vacancy with Ta is practically excluded, in good accordance with electrochemistry (for a discussion of the electrochemical approach, please refer to the SM [54]).

Using one hexagonal unit cell may be a bad model for the highly diluted impurity case since the Ta probes are only separated by  $5.755 \text{ \AA}$  in the horizontal plane. Therefore, we have also done calculations considering one  $2 \times 2 \times 1$  super-

cell. The obtained forces after relaxation were  $<0.03 \text{ eV/\AA}$ . The obtained EFG is  $V_{zz} = 6.21 \times 10^{21} \text{ V/m}^2$  with the PBE approximation and  $5.78 \times 10^{21} \text{ V/m}^2$  with the PBEsol +  $U$  approximation. Using this supercell, we have also performed calculations with charged cells, adding or subtracting 1 and 2 electrons to the neutral state. The results show that, in this case, the defects must be explicitly considered in the calculations of the EFG since it is not very sensitive to the number of electrons used in the calculations:  $V_{zz}$  changes only in the range from  $5.46$  to  $7.10 \times 10^{21} \text{ V/m}^2$ .

An estimation of the EFG change due to the polarization loss as the temperature is increased can be obtained by calculating the Ta:Fe case with a supercell constructed starting from the structure with the  $R\bar{3}c$  space group without the polar distortion. In this case, we obtain  $V_{zz} = 3.93 \times 10^{21} \text{ V/m}^2$  (PBE) or  $3.24$  (PBEsol +  $U$ )  $\times 10^{21} \text{ V/m}^2$ . The decrease of  $V_{zz}$  by almost half when changing from the  $R3c$  to the  $R\bar{3}c$  structure is roughly consistent with the decrease experimentally seen with temperature, suggesting that the main temperature changes can be attributed to a polarization decrease (see case 1 above).

The paraelectric phase at higher temperature has been proposed with orthorhombic  $Pnma$  symmetry [80]. We also calculated the EFG for the probe in this phase, substituting Fe and using a  $2 \times 1 \times 2$  supercell (distance between probes is  $7.89 \text{ \AA}$ ). The results are presented in Table I for both PBE and PBEsol +  $U$  approximations (left and right values). In this structure, the polar mode disappears with respect to the  $R3c$  structure (as in the  $R\bar{3}c$  structure), but there are also new oxygen rotations (with a zone boundary mode  $R_3^+$ ). These different distortion features result in an asymmetric EFG ( $\eta = 0.76$ ), while  $V_{zz}$  is now negative but with absolute value close to the  $R3c$  value. In this case, the transition is first order with a small coexistence temperature region, which would indicate it is not relevant to our measurements (far from the transition temperature  $T_C \sim 1103 \text{ K}$ ).

The result for the case with Ta at the Fe site and an O nearest neighbor removed is  $V_{zz} = 40.96 \times 10^{21} \text{ V/m}^2$  and  $\eta = 0.05$ . The differences are significant but not very large, indicating that this case is close to the highly diluted limit. Cation vacancies are considered already with this dilution, in the case where Ta substitutes for Fe, and the nearest neighbor

Bi (Ta : Fe +  $V_{\text{Bi}}$ ) or Fe (Ta : Fe +  $V_{\text{Fe}}$ ) is removed forming the respective vacancy. These cases yield somewhat more moderate values (Table I). The Fe vacancy case, in addition to having the closest calculated  $V_{zz}$ , also has  $\eta$  close to the experimental value of site 3, while other vacancies produce a nearly axially symmetric EFG. Ultimately, a nearest neighbor cation vacancy is a likely scenario, particularly for an adjacent Fe vacancy (see Table I). This is in good accordance with electrochemistry (see SM [54]).

The calculations presented in Table I were performed assuming ferromagnetic order. However, we also tested two defect configurations with different states with respect to the magnetic order: one where the Fe spins follow the G-AF antiferromagnetic order with the Ta site having a close to zero magnetic moment. The simple substitution Ta : Fe with GGA – PBEsol +  $U = 2$  eV yields  $V_{zz} = 6.10 \times 10^{21}$  V/m<sup>2</sup> ( $\eta = 0$ ); the change of magnetic order—without temperature, as considered in the calculations—does not result in a significant change in the EFG, and the F order should be reasonable.

The calculations shown here are not sufficient to be able to define whether the iron vacancy would reside on the upper or lower triangle in Fig. 1(b). Any site on each triangle is equivalent. The two triangles should yield different  $\eta$  values for the asymmetric site, as the ferroelectric polarization is a vector, and the two triangles then become nonequivalent, but this difference is not resolvable. As spin-orbit coupling is not included in the calculations, they cannot differentiate between the two cases of magnetic easy planes.

Our calculations show that an associated Fe vacancy accounts for a large asymmetry, but the field gradient values do not match as much as we would have expected. All other vacancy configurations yield asymmetry zero, which is also clear from eyesight on the crystal structure. The adjacent iron vacancy is thus also from the modeling point of view the most likely local setting for the asymmetric site 3.

## VI. CONCLUSIONS

Isolated nonmagnetic substitutional defects strongly interact with the electric and magnetic order parameters in BiFeO<sub>3</sub>. The tantalum probe experiences the local electric and magnetic environments. In the ferroelectric temperature range, two local environments are experienced, one representing

substitutional Ta in the iron site, the other an iron vacancy-associated probe ion.

The additional antiferromagnetic order below the Néel temperature generates magnetic-electric combined interaction at the probe site. Due to the high quality of the spectra, the individual magnetic and electric components can be extracted from the fits. Two relative orientations of magnetic order with respect to the EFG tensor axis are found representing the two possible easy planes for magnetic ordering in the material. Magnetic order follows the macroscopic Brillouin function. Due to magnetic ordering, a very large change in local electric environment is found, namely, the electric order is highly distorted around a nonmagnetic probe in BiFeO<sub>3</sub> due to magnetic ordering. If one were to extract a magnetoelectric coupling coefficient from this coupling, it would be extremely large and be at least an order of magnitude larger than known values.

The iron vacancy-associated defect is hardly affected by the long-range order in the material. The vacancy thus seems to decouple the local environment from the magnetic order parameter in the system [85].

Original data are available from the authors upon reasonable request.

## ACKNOWLEDGMENTS

The authors particularly acknowledge funding from the German Federal Ministry of Education and Research (BMBF) through Grant No. 05K16PGA and from Fundação para a Ciência e a Tecnologia (FCT) Project No. CERN-FIS-NUC-0004-2015. We thank the BONIS team at HISKP, Bonn, for the successfully performed <sup>181</sup>Hf implantations. Dr. João Guilherme Martins Correia is thankfully acknowledged for technical support during measurements. The authors thank Astita Dubey for helping with literature scan and discussions and Brahim Dkhil for fruitful discussions.

J.S. did all measurements, initial fits, and wrote the first draft of the paper. Â.R.G.C. helped with measurements. J.N.G. performed the simulations. M.S. and T.T.D. did the final fits and graphics. M.E.C. made the ceramic samples. V.V.S., Î.E. and T.T.D. helped with data interpretation. R.V. and C.N. did the implantations at HISKP in Bonn. U.K. produced the <sup>181</sup>Hf in Grenoble. D.C.L. wrote most of the final text and is responsible for final data interpretation.

- 
- [1] G. Catalan and J. F. Scott, *Adv. Mater.* **21**, 2463 (2009).
  - [2] R. Palai, R. S. Katiyar, H. Schmid, P. Tissot, S. J. Clark, J. Robertson, S. A. T. Redfern, G. Catalan, and J. F. Scott, *Phys. Rev. B* **77**, 014110 (2008).
  - [3] L. A. Shilkina, I. A. Verbenko, A. G. Abubakarov, L. A. Reznichenko, O. N. Razumovskaya, T. N. Sorokun, and V. A. Aleshin, Features of phase formation in the preparation of bismuth ferrite, in *Advanced Materials. Springer Proceedings in Physics*, edited by I. Parinov, S. H. Chang, and V. Topolov (Springer, Cham, 2016), Vol. 175, pp. 79–86.
  - [4] H. Y. Dai, Z. P. Chen, T. Li, R. Z. Xue, and J. Chen, and J. Supercond, *Nov. Magn.* **26**, 3125 (2013).
  - [5] A. M. Kadomtseva, Yu. F. Popov, A. P. Pyatakov, G. P. Vorob'ev, A. K. Zvezdin, and D. Viehland, *Phase Transit.* **79**, 1019 (2006).
  - [6] J.-G. Park, M. D. Le, J. Jeong, and S. Lee, *J. Phys.: Condens. Matter* **26**, 433202 (2014).
  - [7] F. Kubel and H. Schmid, *Acta Cryst. B* **46**, 698 (1990).
  - [8] A. Palewicz, R. Przenioslo, I. Sosnowska, and A. W. Hewat, *Acta Cryst. B* **63**, 537 (2007).
  - [9] P. W. Anderson, *Phys. Rev.* **79**, 705 (1950).
  - [10] A. S. Moskvin, *Hyperfine Interact.* **1**, 265 (1975).
  - [11] I. Gross, W. Akhtar, V. Garcia, L. J. Martínez, S. Chouaieb, K. Garcia, C. Carrétéro, A. Barthélémy, P. Appel, P. Maletinsky *et al.*, *Nature (London)* **549**, 252 (2017).

- [12] T. Moriya, *Phys. Rev.* **120**, 91 (1960).
- [13] D. Lebeugle, D. Colson, A. Forget, M. Viret, A. M. Bataille, and A. Gukasov, *Phys. Rev. Lett.* **100**, 227602 (2008).
- [14] D. Sando, A. Agbelele, D. Rahmedov, J. Liu, P. Rovillain, C. Toulouse, I. C. Infante, A. P. Pyatakov, S. Fusil, E. Jacquet *et al.*, *Nat. Mater.* **12**, 641 (2013).
- [15] S. R. Burns, O. Paull, J. Juraszek, V. Nagarajan, and D. Sando, *Adv. Mater.* **32**, 2003711 (2020).
- [16] J. Silva, A. Reyes, H. Esparza, H. Camacho, and L. Fuentes, *Integr. Ferroelectr.* **126**, 47 (2011).
- [17] R. Das, T. Sarkar, and K. Mandal, *J. Phys. D: Appl. Phys.* **45**, 455002 (2012).
- [18] C.-H. Yang, D. Kan, I. Takeuchi, V. Nagarajand, and J. Seidel, *Phys. Chem. Chem. Phys.* **14**, 15953 (2012).
- [19] Reetu, A. Agarwal, S. Sanghi, Ashima, N. Ahlawat, and Monica, *J. Appl. Phys.* **111**, 113917 (2012).
- [20] V. A. Khomchenko, D. A. Kiselev, M. Kopcewicz, M. Maglione, V. V. Shvartsman, P. Borisov, W. Kleemann, A. M. L. Lopes, Y. G. Pogorelov, J. P. Araujo *et al.*, *J. Magn. Magn. Mater.* **321**, 1692 (2009).
- [21] T. Durga Rao, T. Karthik, and S. Asthana, *J. Rare Earth.* **31**, 370 (2013).
- [22] A. A. Belik, A. M. Abakumov, A. A. Tsirlin, J. Hadermann, J. Kim, G. Van Tendeloo, and E. Takayama-Muromachi, *Chem. Mater.* **23**, 4505 (2011).
- [23] S. M. Selbach, T. Tybell, M.-A. Einarsrud, and T. Grande, *Chem. Mater.* **21**, 5176 (2009).
- [24] K. Chakrabarti, K. Das, B. Sarkar, S. Ghosh, S. K. De, G. Sinha, and J. Lahtinen, *Appl. Phys. Lett.* **101**, 042401 (2012).
- [25] P. Mandal, M. J. Pitcher, J. Alaria, H. Niu, P. Borisov, P. Stamenov, J. B. Claridge, and M. J. Rosseinsky, *Nature (London)* **525**, 363 (2015).
- [26] D. D. Khalyavin, A. N. Salak, N. M. Olekhovich, A. V. Pushkarev, Yu. V. Radyush, P. Manuel, I. P. Raevski, M. L. Zheludkevich, and M. G. S. Ferreira, *Phys. Rev. B* **89**, 174414 (2014).
- [27] N. Wang, J. Cheng, A. Pyatakov, A. K. Zvezdin, J. F. Li, L. E. Cross, and D. Viehland, *Phys. Rev. B* **72**, 104434 (2005).
- [28] R. L. Rasera and G. L. Catchen, *Ferroelectrics* **150**, 151 (1993).
- [29] Y.-K. Jun, S. B. Lee, M. Kim, and S.-H. Hong, *J. Mater. Res.* **22**, 3397 (2007).
- [30] A. W. Carbonari, F. H. M. Cavalcante, R. F. L. Malavasi, G. A. Cabrera-Pasca, J. Mestnik-Filho, and R. N. Saxena, *J. Appl. Phys.* **103**, 07F708 (2008).
- [31] A. M. L. Lopes, G. N. P. Oliveira, T. M. Mendonça, J. A. Moreira, A. Almeida, J. P. Araújo, V. S. Amaral, and J. G. Correia, *Phys. Rev. B* **84**, 014434 (2011).
- [32] G. N. P. Oliveira, R. Teixeira, T. M. Mendonça, M. R. Silva, J. G. Correia, A. M. L. Lopes, and J. P. Araújo, *J. Appl. Phys.* **116**, 223907 (2014).
- [33] A. M. L. Lopes, J. G. Correia, V. S. Amaral, and J. P. Araújo, *Phys. Status Solidi B* **251**, 565 (2014).
- [34] M. Deicher, *Hyperfine Interact.* **79**, 681 (1993).
- [35] A. W. Carbonari, J. Mestnik-Filho, and R. N. Saxena, *Defect Diffus. Forum* **311**, 39 (2011).
- [36] T. Wichert and E. Recknagel, Microscopic methods in metals, in *Topics in Current Physics*, edited by U. Gonser (Springer Verlag, Heidelberg, New York, 1986), Vol. 40, p. 317.
- [37] J. Schell, D. C. Lupascu, A. W. Carbonari, R. D. Mansano, I. S. Ribeiro Jr., T. T. Dang, I. Anusca, H. Trivedi, K. Johnston, and R. Vianden, *J. Appl. Phys.* **121**, 145302 (2017).
- [38] K. Johnston, J. Schell, J. G. Correia, M. Deicher, H. P. Gunnlaugsson, A. S. Fenta, E. David-Bosne, A. R. G. Costa, and D. C. Lupascu, *J. of Phys. G: Nucl. Particle Phys.* **44**, 104001 (2017).
- [39] G. Schatz and A. Weidinger, *Nuclear Condensed Matter Physics: Nuclear Methods and Applications* (Wiley, Chichester, 1996).
- [40] H. Frauenfelder, R. M. Steffen, and K. Siegbahn, *Alpha-, Beta-, and Gamma-Ray Spectroscopy*, edited by K. Siegbahn, Vol. 2 (Elsevier, Amsterdam: North-Holland, 1968), Chap. XIX, pp. 997–1044.
- [41] A. Abragam and R. V. Pound, *Phys. Rev.* **92**, 943 (1953).
- [42] A. F. Pasquevich and R. Vianden, *Phys. Rev. B* **35**, 1560 (1987).
- [43] W. Bolse, M. Uhrmacher, and K. P. Lieb, *Phys. Rev. B* **36**, 1818 (1987).
- [44] T. Butz, *Hyperfine Interact.* **52**, 189 (1989).
- [45] M. Forker, *Nucl. Instr. Meth.* **106**, 121 (1973).
- [46] T. Butz, S. K. Das, and Y. Manzhur, *Z. Naturf. A* **64a**, 103 (2009).
- [47] X. Wang, S. Y. Wang, W. F. Liu, F. Guo, X. J. Xi, H. J. Wang, and D. J. Li, *Modern Phys. Lett. B* **28**, 1450050 (2014).
- [48] D. Lupascu, S. Habenicht, K. P. Lieb, M. Neubauer, M. Uhrmacher, and T. Wenzel, *Phys. Rev. B* **54**, 871 (1996).
- [49] E. J. Konopinski and M. E. Rose, *Alpha-, Beta-, and Gamma-Ray Spectroscopy*, edited by K. Siegbahn (Elsevier North-Holland, Amsterdam, 1968). Vol. 2, Chap. XXIII, Sec. 6, p. 1357.
- [50] R. L. Rasera and G. L. Catchen, *Phys. Rev. B* **58**, 3218 (1998).
- [51] <http://www.cas.miamioh.edu/~jaegerh/kn.htm>.
- [52] E. Matthias, W. Schneider, and R. M. Steffen, *Phys. Rev.* **125**, 261 (1962).
- [53] K. Alder, E. Matthias, W. Schneider, and R. M. Steffen, *Phys. Rev.* **129**, 1199 (1963).
- [54] See Supplemental Material at <http://link.aps.org/supplemental/10.1103/PhysRevB.105.094102> for XRD spectra of the BiFeO<sub>3</sub> ceramics, Fourier transforms of the PAC spectra, the fit to Landau function, Hf-ion incorporation into BiFeO<sub>3</sub>, hard versus soft doping, decay of <sup>181</sup>Hf, and differential scanning calorimetry, and it includes Refs. [81–84].
- [55] G. Marschick, J. Schell, B. Stöger, J. N. Gonçalves, M. O. Karabasov, D. Zyabkin, A. Welker, M. C. Escobar, D. Gärtner, I. Efe, R. A. Santos, J. E. M. Laulainen, and D. C. Lupascu, *Phys. Rev. B* **102**, 224110 (2020).
- [56] K. Freitag, *Radiat. Eff.* **44**, 185 (1979).
- [57] N. J. Stone, *Atom. Data Nucl. Data* **111–112**, 1 (2016).
- [58] A. Jancso, J. G. Correia, A. Gottberg, J. Schell, M. Stachura, D. Szunyogh, S. Pallada, D. C. Lupascu, M. Kowalska, and L. Hemmingsen, *J. Physics G: Nucl. Particle Phys.* **44**, 064003 (2017).
- [59] M. Jäger, K. Iwigand, and T. Butz, *Rev. Sci. Instr.* **82**, 065105 (2011).
- [60] NIGHTMARE (MDI) Version RC 3 (1.2.0.247). Copyright (2005–2010) from the group Reiner Vianden and (2008–2010) Ronan Nédélec, Bonn University.

- [61] J. N. Gonçalves, A. Stroppa, J. G. Correia, T. Butz, S. Picozzi, A. S. Fenta, and V. S. Amaral, *Phys. Rev. B* **86**, 035145 (2012).
- [62] M. E. Lines and A. M. Glass, *Principles and Applications of Ferroelectrics and Related Materials* (Clarendon Press, Oxford, 1977).
- [63] B. A. Strukov and A. P. Levanyuk, *Ferroelectric Phenomena in Crystals: Physical Foundations* (Springer, Berlin, Heidelberg, 1998).
- [64] D. V. Karpinsky, E. A. Eliseev, Fei Xue, M. V. Silibin, A. Franz, M. D. Glinchuk, I. O. Troyanchuk, S. A. Gavrilov, V. Gopalan, Long-Qing Chen, and A. N. Morozovska, *npj Comp. Materials* **3**, 20 (2017).
- [65] R. D. Shannon, *Acta Cryst.* **A32**, 751 (1976).
- [66] J. Seidel, L. W. Martin, Q. He, Q. Zhan, Y.-H. Chu, A. Rother, M. E. Hawkrige, P. Maksymovych, P. Yu, M. Gajek *et al.*, *Nat. Mater.* **8**, 229 (2009).
- [67] C. Blaauw and F. van der Woude, *J. Phys. C: Solid State Phys.* **6**, 1422 (1973).
- [68] P. Fischer, M. Połomska, I. Sosnowska, and M. Szymański, *J. Phys. C: Solid State Phys.* **13**, 1931 (1980).
- [69] J. Landers, S. Salamon, M. Castillo Escobar, D. C. Lupascu, and H. Wende, *Nano Lett.* **14**, 6061 (2014).
- [70] W. Ratcliff II, Z. Yamani, V. Anbusathaiah, T. R. Gao, P. A. Kienzle, H. Cao, and I. Takeuchi, *Phys. Rev. B* **87**, 140405(R) (2013).
- [71] W. Saenrang, B. A. Davidson, F. Maccherozzi, J. P. Podkaminer, J. Irwin, R. D. Johnson, J. W. Freeland, J. Íñiguez, J. L. Schladt, K. Reiersen *et al.*, *Nature Commun.* **8**, 1583 (2017).
- [72] K. Miura, M. Azuma, and H. Funakubo, *Materials* **4**, 260 (2011).
- [73] A. Grünebohm, M. Marathe, R. Khachatryan, R. Schiedung, D. C. Lupascu, and V. V. Shvartsman, *J. Phys.: Condens. Matter* **34**, 073002 (2022).
- [74] P. E. Blöchl, *Phys. Rev. B* **50**, 17953 (1994).
- [75] G. Kresse and J. Furthmüller, *Phys. Rev. B* **54**, 11169 (1996).
- [76] J. P. Perdew, K. Burke, and M. Ernzerhof, *Phys. Rev. Lett.* **77**, 3865 (1996).
- [77] J. P. Perdew, A. Ruzsinszky, G. I. Csonka, O. A. Vydrov, G. E. Scuseria, L. A. Constantin, X. Zhou, and K. Burke, *Phys. Rev. Lett.* **100**, 136406 (2008).
- [78] S. L. Dudarev, G. A. Botton, S. Y. Savrasov, C. J. Humphreys, and A. P. Sutton, *Phys. Rev. B* **57**, 1505 (1998).
- [79] J. K. Shenton, D. R. Bowler, and W. L. Cheah, *J. Phys.: Condens. Matter* **29**, 445501 (2017).
- [80] D. C. Arnold, K. S. Knight, F. D. Morrison, and P. Lightfoot, *Phys. Rev. Lett.* **102**, 027602 (2009).
- [81] L. L. Hench and J. K. West, *Principles of Electronic Ceramics* (John Wiley & Sons, New York, 1990).
- [82] N. Setter and E. L. Colla, *Ferroelectric Ceramics: Tutorial Reviews, Theory, Processing, and Applications* (Birkhaeuser Verlag, Basel-Boston-Berlin, 1993), pp. 65–66.
- [83] U. Robels and G. Arlt, *J. Appl. Phys.* **73**, 3454 (1993).
- [84] S. M. Selbach, T. Tybell, M.-A. Einarsrud, and T. Grande, *Adv. Mater.* **20**, 3692 (2008).
- [85] D. Lebeugle, A. Mougin, M. Viret, D. Colson, and L. Ranno, *Phys. Rev. Lett.* **103**, 257601 (2009).

*Correction:* The copyright license statement was presented incorrectly and has been fixed.